ACCSCIENCE PUBLISHING

International Journal of Bioprinting

RESEARCH ARTICLE

Development of a low-cost quad-extrusion 3D bioprinting system for multi-material tissue constructs

Ralf Zgeib, Xiaofeng Wang, Ahmadreza Zaeri, Fucheng Zhang, Kai Cao, and Robert C. Chang*

Department of Mechanical Engineering, Stevens Institute of Technology, Hoboken, New Jersey, USA

(This article belongs to the *Special Issue: 3D Bioprinting Hydrogels and Organ-On-Chip*)

Abstract

This study presents the development and characterization of a low-cost bioprinting system with a compact low-profile quad-extrusion bioprinting head for producing multi-material tissue constructs. The system, created by modifying an off-the-shelf three-dimensional (3D) printer, enables larger print volumes compared to extant systems. Incorporating gelatin methacrylate (GelMA) as a bioink model, the bioprinting system was systematically tested with two different printing techniques, namely the traditional in-air printing (IAP) mode along with an emerging support bath printing (SBP) paradigm. Structural fidelity was assessed by comparing printed structures under different conditions to the computer-aided design (CAD) model. To evaluate biological functionality, a placental model was created using HTR-8 trophoblasts known for their invasive phenotype. Biological assays of cell viability and invasion revealed that the cells achieved high cell proliferation rates and had over 93% cell viability for a 3-day incubation period. The multi-compartmental 3D-bioprinted *in vitro* placenta model demonstrates the potential for studying native cell phenotypes and specialized functional outcomes enabled by the multi-material capability of the quad-extrusion bioprinter (QEB). This work represents a significant advancement in bioprinting technology, allowing for the printing of complex and highly organized tissue structures at scale. Moreover, the system's total build cost is only US$ 297, making it an affordable resource for researchers.

Keywords: 3D bioprinting; Quad-extruder; Multi-material; Support bath printing; GelMA; Laponite B

***Corresponding author:**
Robert C. Chang
(rchang6@stevens.edu)

Citation: Zgeib R, Wang X, Zaeri A, *et al*., 2023, Development of a low-cost quad-extrusion 3D bioprinting system for multi-material tissue constructs. *Int J Bioprint*. https://doi.org/10.36922/ijb.0159

Received: May 10, 2023
Accepted: June 29, 2023
Published Online: August 29, 2023

1. Introduction

Additive bio-manufacturing (bio-AM), or three-dimensional (3D) bioprinting, has emerged as a prevailing tool in the development of complex programmable tissue constructs[1-6]. 3D bioprinting enables diverse *in vitro* biological studies for medicinal studies of pathological conditions by creating microenvironments suitable for cells to form tissues that are functionally equivalent to the *in vivo* scenario[7-10]. Ultimately, with fully developed 3D-bioprinted biological constructs made with multiple bioinks, full organ transplantation would be possible[11-17]. More recently, complex 3D bioprinting

with multiple materials is achieving more popularity and pertinence in several fields of use, including *in vitro* meat development as an alternate food source that helps in reducing methane gas release into the atmosphere resulting from animal carnage. These engineered meats are composed of multiple tissue types embedded within a single construct to mimic the natural architecture of a Wagyu beef steak which is essential in developing the proper taste and quality of meat[18,19].

Available bioprinting technologies that enable multi-material printing for diverse biological studies are very complex and rarely allow more than two or three materials to be printed in a single construct. However, with multi-material bioprinter designs, the cost remains prohibitively high, rendering the scalability of such technologies to be a significant challenge[20-23]. Of all the available bioprinting technologies, extrusion-based systems are the most prominent for multi-material printing due to the ease of development and modularity[24,25]. For example, Shen *et al.* developed a Computer Numerical Control (CNC)-based bioprinter that has four separate extruders and allows multi-material bioprinting. However, it costs around US$ 6000, which is still considered along the higher end of prices with the current technologies available[26]. Several efforts have been made to design and develop low-cost and ultra-low-cost bioprinters based on reliable process designs at costs not exceeding US$ 200–250[27-34]. For a more detailed overview, **Table S1** (Supplementary File) compiles an overview of both commercial bioprinters currently available on the market and relevant research endeavors, specifically focusing on those positioned within the more affordable cost range. Although with extant low-cost process designs available, limited functionality is achieved. Notably, the characteristic bulky and complex nozzle designs that typify existing low-cost bioprinters effectively limit the reach and range of tissue applications. This fundamental limitation can be attributed to the significant loss or reduction in printing volumes, even with single or dual nozzle configurations. This limits the range of tissue types and sizes that can be printed with such small printing volumes and a limited number of material nozzles. On the one hand, the present design configurations limit the ability to advance a low-cost bioprinting system capable of fabricating more complex tissue constructs with multi-materials at arbitrary scales. On the other hand, by endowing a bioprinter with large-scale multi-material capability, the application range can be extended to include investigations into the interactions between multiple bioinks with different cellularized matrix content and organization that define the tissue mechanical properties. Specifically, investigations into the bioink material–material interfaces that join disparate target tissues, along with cell–material and cell–cell interaction studies, are crucial in promoting more realistic *in vitro* tissue models that better mimic *in vivo* tissue models and, ultimately, closing the scalability gap toward fully functional organ printing[35].

In this work, a commercial off-the-shelf (COTS) fused deposition modeling (FDM) 3D printer was systematically mass-modified with a novel quad-extrusion head (QEH) that is compact with a low profile, thereby minimizing its moment of inertia when in motion. The quad-extrusion bioprinter (QEB) was rendered at a relatively low overall cost of US$ 297, proving to be a reliable low-cost bioprinter with versatile capabilities. With that, it becomes possible to fabricate multi-material biological constructs, thereby widening the scope and accessibility of *in vitro* studies. This is enabled by the large printing volumes that the QEB affords, which provides the capability to create tissue constructs at scale. Moreover, with its developed compact and low-profile design, the QEH module is transferable to other FDM 3D printers typified by similar frame designs, with minor modifications to the extruder carrier. To demonstrate the capabilities of the developed QEB, gelatin methacrylate (GelMA) bioink[36] was used as a biomaterial model to print complex multi-material constructs using two printing paradigms. One paradigm is the more traditional in-air printing (IAP), where the bioink is printed on glass slides or petri dishes suspended only in air. Alternatively, the second paradigm is support or suspension bath printing (SBP), where the bioink is printed in a bath of nanoclay that can self-support the bioprinted material[37]. The nanoclay bath used in this work was Laponite B. HTR-8 SV/neo trophoblasts were implemented as a biological model to validate the functionality of the bioprinted hydrogel structures in providing a suitable environment for the cells to perform their intended function. Finally, post-process structural and biological characterizations of the bioprinted constructs were performed by way of assessing geometric fidelity and cell proliferation and viability by way of microscopic imaging of the fluorescently labeled construct.

2. Materials and methods

2.1. Bioprinter components

To develop the in-house bioprinter with the QEH, several components were directly bought as COTS. As a start, a Creality Ender 3 Pro 3D printer was purchased off Amazon for US$ 209. However, with the stock controller, there is only one pin for a single extruder. To be able to control four extruders at the same time, the Zonestar ZRIB V6 control board was purchased to replace the stock control board and allow the control of four independent extruder stepper motors. The Zonestar controller board costs US$

49, and the additional three stepper motors cost US$ 19, making the total cost of COTS materials and 3D-printed parts to be approximately US$ 297. This represents a very low price point for a quad-extrusion 3D bioprinting system compared to what has thus far been reported in the literature. A detailed table of components can be found in the GitHub repository mentioned in the Availability of data section.

2.2. QEH design and QEB development

The QEH was designed and developed in-house using Autodesk Fusion 360, where all motions and tolerances were simulated to verify the proper functioning of the system. With the compactness of this minimalistic low-profile design, the maximization of printing volumes with functionally biomimetic characteristics was achieved.

The fabrication of the main body of the QEH was done in-house using an FDM 3D printer with PLA+ filament (DURAMIC 3D, Amazon, USA). This allows the maintenance of the tight tolerances desired and minimizes any warping within the model[38]. The gears and syringe plunger holders were printed with acrylonitrile butadiene styrene (ABS) to ensure high strength within those parts since they are moving parts with high torque exerted on them.

To properly control the QEH, the appropriate firmware configurations need to be developed. For that purpose, the open-source Marlin 2.0.3 firmware (MarlinFirmware/Marlin, GitHub) was adopted and modified to suit the physical properties and requirements of our bioprinting system (GitHub link can be found in the Availability of data section). Namely, the firmware was made to accommodate four extruders and allow cold extrusion by setting a dummy temperature sensor to compensate for the removal of the existing temperature sensor. The modified firmware was then uploaded to the upgraded motherboard, and the step motors were calibrated to output the correct number of turns and speeds as needed. This allowed the control of the QEB through any open-source control software, namely Repetier Host (Repetier-Host, Repetier) used herein.

The g-code generated needed to be customized based on the machine and the model being printed. Starting and ending g-codes as well as the extruder change g-code were added into the slicer to modify the generated g-code based on the type of printing paradigm being adopted (IAP versus SBP). The starting Z-level was also modified to meet the desired starting height based on each type of substrate.

2.3. Biological studies

2.3.1. Cell culture and fluorescence staining

HTR-8/SVneo (HTR-8) derived from the SV40-transfected first trimester EVT cell line (ATCC, USA) were cultured in DMEM/F12 medium containing 5% fetal bovine serum (FBS), 1% penicillin–streptomycin solution, and 0.5% neomycin. The cells were then stored in a humidified 5% CO_2 incubator at 37°C. Before mixing the cells with GelMA, cells were stained with green fluorescence using CFDA-SE (CFDA-SE, Invitrogen, CA, USA) to track their proliferation and migration within the final printed constructs using a wide-field fluorescence microscope (IX83P1ZX, Olympus, TYO, JP).

2.3.2. Viability and invasion assays

The steps done by Zhu *et al.* were followed exactly for conducting viability assays[39]. LIVE/DEAD staining kits (LIVE/DEAD Viability/Cytotoxicity Kit, Invitrogen, CA, USA) were used. Tissue constructs were washed with Dulbecco's phosphate-buffered saline (DPBS) and stained with 2 μM calcein blue AM (green stain for live cells) and 4 μM ethidium homodimer-1 (red stain for dead cells) solution and then incubated for 30 min. After incubation, the stained constructs were washed and imaged under the wide-field microscope with fluorescein isothiocyanate (FITC; green stain for live cells) and tetramethylrhodamine (TRITC; red stain for dead cells) channels. The images were then analyzed using ImageJ for cell counting and viability results.

To characterize the function of cells in bioprinted tissue constructs, a trophoblast (HTR-8) invasion assay in a simplified 3D-bioprinted placenta model was performed. The placenta model was printed with four different bioinks using IAP for ease of culturing and the lack of necessity of post-processing. Figure 6A shows a top-view design of the placenta model. This model is composed of two main modules, the epidermal growth factor (EGF) (EGF/Alexa-555 conjugate, ThermoFisher, USA) and the HTR-8 modules. All sections of the model are composed of GelMA bioinks. The two modules were separated by two main channels that allow us to study the invasion of the HTR-8 cells from the cell module to the EGF module. The two main channels are the control channel, which is composed only of GelMA, and the experimental model, which comprises GelMA and a low concentration of EGF. To ensure that the cells invade only through the control and experimental channels at the same conditions, GelMA separation channels, made of 10% GelMA, were added and highly crosslinked. This would make those separation channels stiffer and harder for cells to invade through. To ensure that the cells do not migrate to the surface or bottom of the bioprinted modules, highly crosslinked GelMA bed and cap layers were added below and above the modules, respectively, as shown in Figure 6B. With this model configuration, cells would only invade through the designated channels where the effect of EGF on cell

invasion can be studied. FITC and TRITC fluorescence images were taken after 30 h of incubation to visualize the CFDA-SE-stained HTR-8 cells in green and the EGF/Alexa-555 conjugate in red, respectively.

2.4. Bioink preparation

GelMA bioinks were prepared akin to the method described in Ding *et al.*[40] with minor differences based on the recommendations of the biomaterial vendor. First, lithium phenyl-2,4,6-trimethylbenzoylphosphinate (LAP; Allevi Inc., PA, USA) was fully dissolved in DPBS at 60°C for 15–30 min with a 0.5% w/v concentration of the final bioink solution. It is important to keep the solution in an amber container or covered with aluminum foil to prevent contact with light and premature photoinitiator activation. When the LAP was fully dissolved in the DPBS solution, lyophilized gelMA foam (GelMA, Allevi Inc., PA, USA) was added to the solution with a 10% w/v final concentration. The final mixture was thoroughly mixed at 60°C for over an hour in the dark. It is noteworthy that the material preparation was performed under a sterile biohood to minimize contamination. When the as-prepared GelMA bioink mixture was well dissolved and homogenized, it was stored overnight in the dark at 4°C. For cell-free bioprinting, GelMA was melted down in a warm water bath (37°C), diluted in DPBS to the desired concentration, and mounted in a 3 mL syringe that was covered with aluminum foil to maintain the prevention of any premature crosslinking before and during printing.

For the cell-laden bioink formulation, melted GelMA was sterile-filtered in two stages using sterile filters with pores sizes of 0.45 μm and 0.20 μm, sequentially. The sterile GelMA was then mixed with a cell pellet mixed in cell media in volumes that would render a certain desired final bioink concentration. For the advanced case study herein, due to their availability, HTR-8/SVneo cells were used after being centrifuged at 300 rpm for 5 min. The cell pellet was mixed with cell media, which was then mixed by gently pipetting with the melted sterile GelMA to reach a final concentration of 5% cell-laden GelMA bioink with approximately 2×10^6 cells mixed therein.

2.5. Support bath material preparation

The support bath material (SBM) is prepared from Laponite nanoclay ($Na_{0.7}Si_8Mg_{5.5}Li_{0.3}O_{20}(OH)_4$) that creates a yield stress bath that can self-support the printed bioink inside. The Laponite nanoclay was prepared following the manufacturer's recommendations as well as the steps undertaken by Ding *et al.*[40] The SBM tested was Laponite B (BYK Additives Inc., Gonzales, TX, USA). The nanoclay powder was slowly and continuously added to a beaker with deionized water, and it was then vigorously stirred for 24 h to ensure proper dispersion in the final solution. Since the printed bioink is GelMA and does not require chemical crosslinking, no $CaCl_2$ was added to the solution as would be the case with alginate. The Laponite B concentration adopted was 1.5% (w/v).

2.6. 3D bioprinting, ultraviolet crosslinking, and post-processing of printed bioinks

To prepare the toolpath g-codes of the computer-aided design (CAD) models to be printed, Cura (Cura, Ultimaker, USA) was used to slice the CAD models and obtain the toolpath for printing. However, to accommodate the physical characteristics of our QEB, custom starting and ending g-code modifications are needed to avoid physical interference. These modifications also need to be customized based on the type of substrate used to print on, in the case of IAP, or within, in the case of SBP.

Before bioprinting, warm (room temperature) cell-free or cell-laden bioinks were filled into 3 mL syringes. The syringes were equipped with 2-inch 23G nozzles (Nordson EFD, RI, USA) and were covered with aluminum foil to prevent premature crosslinking. The prepared bioink syringes were then mounted onto the QEH. To ensure the alignment of the four nozzle tips along the z-direction, a specific point on the print bed grid was identified, and the four nozzles were zeroed along the z-levels by simply turning the needle tips along with the Luer locks. This is necessary since the four nozzles are in-line and may interfere with the printed structures.

To crosslink the bioprinted gelMA bioinks, a handheld 8 Watt, 365 nm ultraviolet (UV) light (UVP, UVL-18 365 nm UV light, Analytik Jena US, CA, USA) was used in the case of IAP. The UV lamp was placed on top of the petri dish, covering the whole area of the bioprinted sample. Since the size and shape of the UV lamp are rectangular, wide, and long enough to cover the whole substrate being printed on, it is safe to assume uniform crosslinking has occurred within the samples. However, for the case of SBP, the beaker carrying the support bath, along with the printed construct, was placed in a UV curing station (Sovol 3D SL1 Curing Station, Amazon, USA) that has UV light strips on the sides and the top while being completely mirror-polished on the inside with a turntable in the center of the bottom plate. This ensures a uniform omnidirectional UV light dispersion within the mirrored curing box allowing uniform crosslinking of the bioprinted samples in the support bath. The distance would vary depending on the size and geometry of the bioprinted sample. Crosslinking times were varied based on the desired final stiffness of the bioprinted constructs. The crosslinking process was either done simultaneously throughout the printing process or at a single instance during post-processing, depending on the printing

paradigm used. For SBP, the final bioprinted structures were crosslinked at the end at once. On the other hand, for IAP, depending on the GelMA bioink concentration, the structures were either crosslinked during printing or post-processing. Low-concentration GelMA bioinks (less than 5% w/v) were crosslinked continuously or periodically during bioprinting upon the change of the printing nozzles. This was done to maintain the structures as printed and to allow clear interfaces with no mixing between different bioinks that come in contact with each other. In contrast, with bioinks of high concentration, crosslinking was performed at the end of the bioprinting process since the bioinks can maintain the structure without failure or mixing at the interfaces.

In the case of SBP, post-processing extraction of the crosslinked constructs from the SB is required. The SB containing the bioprinted construct was immersed in a DPBS container with a magnetic bar. The DPBS container including the SB was then subjected to magnetic stirring. Light stirring allowed the SBM to smoothly and quickly dissolve, releasing the bioprinted construct into the DPBS bath. This allowed the extraction to occur with minimal or no structural damage caused or viability loss.

2.7. Statistical methods

Experimental data were analyzed with GraphPad Prism (GraphPad Software, CA, USA) using one-way analysis of variance (ANOVA) with repeated measures to test the significance between the sets of each parameter with the Tukey–Kramer *post-hoc* test. All data are expressed as mean ± standard deviation. Significance was considered when $^{*}p < 0.05$, $^{**}p < 0.01$, and $^{***}p < 0.001$.

3. Results

The QEH developed was installed onto the commercial FDM 3D printer with all necessary modifications. This renders a low-cost QEB that is capable of printing multi-material constructs for biological tissue studies. The whole system costs approximately US$ 297 and is transferrable to any other commercial FDM 3D printer with minor modifications of the fixture. The QEB has an overall bounding box dimension of 410 × 430 × 465 mm, making it suitable for functioning inside a laminar flow biohood. The QEB's capabilities were then demonstrated through a set of prints of simple and complex multi-material constructs using SBP and IAP paradigms. Finally, structural fidelity as well as cell viability and function of those prints were assessed. HTR-8/SVneo cells were used as a model example for cell-laden bioinks printed with the advanced QEB herein. No other bioprinting system has yet to be reported to provide the stated capabilities at this low cost and adaptability across different bio-AM systems.

3.1. Quad-extrusion bioprinter specifications

To develop the QEB, a low-cost, robust, and well-support Ender 3 Pro desktop 3D printer was purchased to use the strong compact open frame design it offers. The open-frame design enables facile modification of the printer with the QEH developed. The assembly of the entire printer frame took approximately 10 min, as it came partially pre-assembled, and the assembling only required the joining of the base to the vertical frame with four screws and the connection of three wires. The regular 3D printer extruder was swapped with the assembled QEH simply using four screws that attach to the stock extruder carrier. The dimensions and tolerances of the QEH were precisely designed to accommodate the printer frame easily, as the full 3D model of that printer is freely available online. The Ender 3 Pro has a printing volume of 220 × 220 × 250 mm and a printing resolution of 12 μm and 4 μm in the *X*–*Y* and *Z* directions, respectively. This is the specified manufacturer rating based on the type of stepper motors, timing belts, and lead screw rods used. They indicate the minimum distances that each axis can move but do not indicate the printing accuracy and shape fidelity of the bioprinted constructs.

The QEH was designed to accommodate four stepper motors fixed closely together as low as possible near the QEH fixation location. This renders a compact and low-profile design with minimal moment of inertia. This design also helps minimize instability due to the jerk and acceleration of the QEH as prints are ongoing. With this setup, the available printing volume was maximized with this efficient and compact design. The printing volume achievable was measured with the different number of extruders used. The printing volume limits were measured between the reachable overlapping extremes of the QEH when printing with one, two, three, or four extruders simultaneously. In addition to the achievable printing volumes, the ranges of functions of the different parameters attainable with the QEB are summarized in Table 1.

The changes leading to the final QEB design can be seen in Figure 1. The original stock Creality Ender 3 Pro is shown in Figure 1A. The stock extruder and motherboard were removed, and the ZONESTAR ZRIB V6 motherboard was installed (Figure 1B). The final fully assembled QEB CAD model in Figure 1C illustrates the newly designed QEH with its syringe frame (Figure 1D) mounted on the printer's *X*-axis. Figure 1E shows the variable Z-limit switch mechanism developed. **Figure S1** (Supplementary File) shows further development stages with regard to the QEH.

3.2. 3D bioprinting outcomes using IAP and SBP

In order to demonstrate the capabilities of the QEB with IAP, several multi-material models were printed as shown

Table 1. Attainable range of function of the different parameters of the QEB

Parameter	Achievable range of function
Printing volume (printing mode; % of original print volume)	220 × 210 × 250 mm (Single extrusion mode; 95.5%) 175 × 210 × 200 mm (Dual extrusion mode; 63.6%) 145 × 210 × 200 mm (Triple extrusion mode; 52.7%) 115 × 210 × 200 mm (Quad-extrusion mode; 41.8%)
Speed	1–12 mm/s
Layer thickness	0.1–1 mm (depending on nozzle diameter; 17G–27G needle tips)
Temperature	20–40°C (depending on bioink concentration)
Viscosity	30–6 × 10^7 mPa·s[45]
Bioink concentration	3%–20% (for GelMA bioinks)

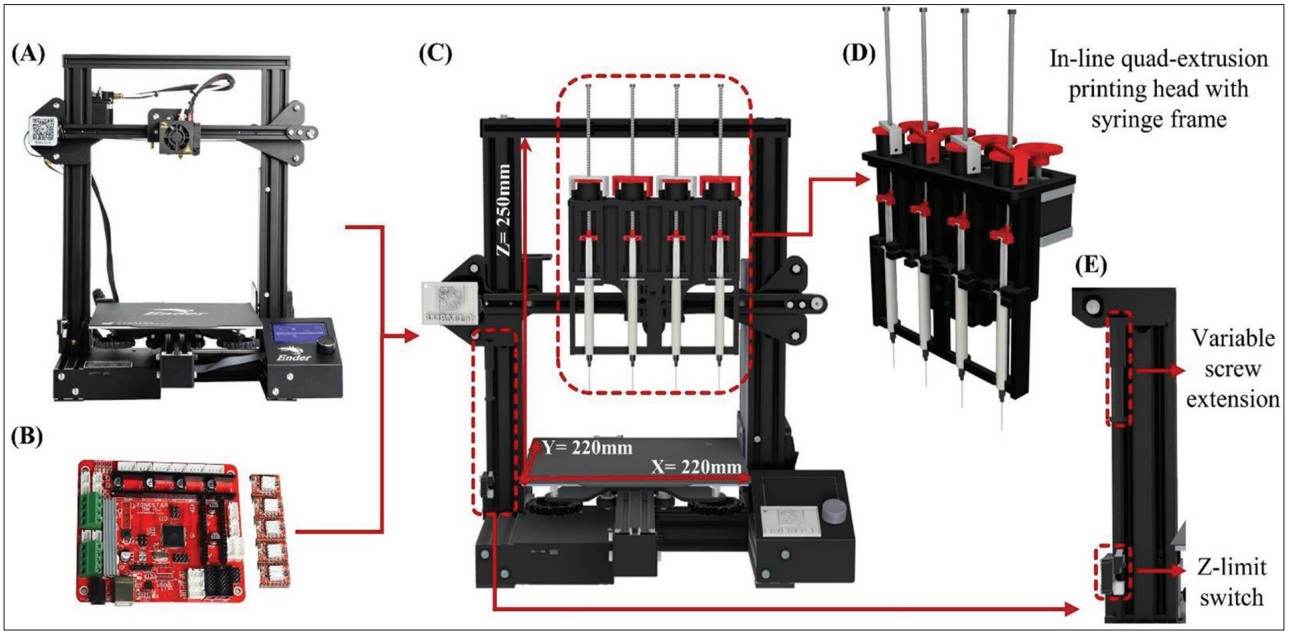

Figure 1. QEB development and components. (A) Original Creality Ender 3 Pro desktop 3D printer. (B) ZONESTAR ZRIB V6 motherboard. (C) Final QEB 3D CAD model showing the modifications done on the Ender 3 Pro with the final QEH mounted on the printer. (D) Final QEH with the added nozzle frame to maintain nozzle alignment. (E) Variable screw extension for Z-limit switch for different needle length accommodation.

in Figure 2. The bioinks used were GelMA bioinks colored with different food coloring to allow the visualization of the different bioinks. Five percent GelMA was used for all the structures except for the ones printed with 10% gelMA as shown in Figure 2E. Only single (Figure 2B and C) and two-layer (Figure 2A) structures were printed with 5% GelMA due to the difficulty of going up with layer height at such low concentrations of bioinks. It can be noted that, with IAP and low-concentration bioinks, sharp edges and boundaries were slightly inconsistent as Figure 2D-ii shows. Slight mixing at the different bioink interfaces also occurred, as Figures 2B-ii and C-ii show. In Figure 2E, the printed hollow 10 × 10 × 10 mm cube showed that it was possible to print water-tight structures with IAP and higher concentration bioinks. This was proven by the addition of the blue-dyed water to the hollow cube shown in Figure 2E-iii. For context, advanced bioinks for complex water-tight structures have been previously considered[41].

Moreover, to demonstrate the capabilities of the QEB beyond IAP, several more complex models were printed using SBP techniques. SBP is particularly useful when printing complex models that are hard to print with IAP. Boundary preservation and interfacial mixing are overcome, as well as high layer numbers are easily achieved even with low-concentration bioinks. Figure 3 shows the different toolpaths and the resulting prints in the support bath. It is clear how boundaries of the different structures were preserved and minimal mixing between the different bioinks happened. Figure 3A is the toolpath of a four-way intersection network of hollow tubes, representing a capillary network. Each network branch is printed with a

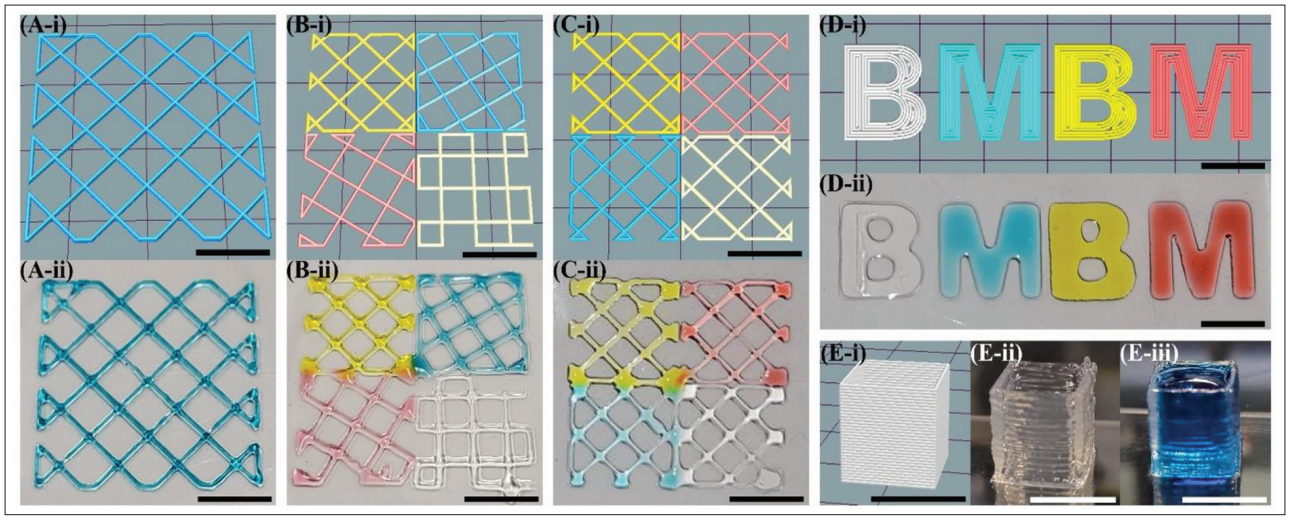

Figure 2. In-air Printing (IAP) toolpaths and prints. (A-i) G-code of a 3 × 3 cm 2-layer single-material grid. (A-ii) Printed 3 × 3 cm 2-layer single print grid. (B-i) G-code of 4 multi-material 1.5 × 1.5 cm single-layer grids with different line orientations. (B-ii) Printed 4 multi-material 1.5 × 1.5 cm single-layer grid with different orientations. (C-i) G-code of 4 multi-material 1.5 × 1.5 cm single-layer grids with the same line orientation. (C-ii) Printed 4 multi-material 1.5 × 1.5 cm single-layer grid with the same line orientation. (D-i) G-code of a single-layer BMBM lab signage in 4 different materials. (D-ii) Printed single-layer BMBM lab signage in 4 different materials. (E-i) G-code of a 1 × 1 × 1 cm single-material hollow cube. (E-ii) Printed 1 × 1 × 1 cm single-material hollow cube. (E-iii) 1 × 1 × 1 cm single-material hollow cube filled with blue-dyed water showing watertight structure (scale bar = 1 cm applies to all images).

different bioink. Figure 3B displays a stack of four hollow cylinders made from four different bioinks, representing an arterial structure that can be composed of different types of tissues. Also, Figure 3C shows a multi-material concentric cylinder structure that mimics the interfacial layering of certain tissues in the body. Moreover, as shown in Figure 3D, the research lab signage (BMBM) was printed for comparison with that printed with IAP. It can be observed that the boundaries and edges were better preserved with SBP compared to IAP. The dimensions of the letters and whole structure were more accurate and compliant with the designed toolpath. Finally, as shown in Figure 3E, a trifurcation structure composed of four different materials was printed. This is a representation of a capillary 3-to-1 junction that can be found in an *in vivo* capillary network. The trifurcation was then crosslinked and extracted from the support bath. Due to photobleaching, all the different colors disappeared, ultimately yielding a homogeneous color and structure.

3.3. 3D printing characterization

It is important to properly characterize the printed outcome of the bioprinter to ensure that they can properly perform their intended functions. Structural and biological characterizations are performed herein to validate the printing outcomes of the developed QEB.

3.3.1. Structural fidelity or compliance

In order to characterize the structural outcome of the 3D-printed structures using the QEB, single-layer grid structures (similar to the grid seen in Figure 2A) were printed and the strand widths were measured using ImageJ and compared to the design parameters. The printed grids, composed of 5% gelMA bioink, were constructed under different conditions of temperatures, UV-crosslinking, and printing techniques. In Figure 4, the mean width measurements are plotted as bar graphs and compared to the designed stand width of 0.45 mm, which is visualized by the first green bar in each graph.

Specifically, Figures 4A and B show the effect of temperature by comparing the average strut widths of grids printed at 25°C and 30°C. It is clear that at 25°C, the average strut width did not significantly change compared to those printed at 30°C, especially those printed using SBP. The average increase in strut width increased from a range of 5.6%–33.7% at 25°C to a higher range level of 27.7%–40.9% at 30°C. As shown in Figure 4C and D, the effect of the printing paradigm was realized by looking at the difference between IAP and SBP. The average increase in strut width decreased significantly from a range of 30.4%–40.9% with IAP to a much lower range of 5.6%–38.2% with SBP. In Figure 4E and F, the effect of UV crosslinking is shown. Although the difference between the measurements before and after UV crosslinking was not very significant, the average strut width was still slightly decreased after crosslinking, approaching the desired designed width. Normalized values of the strand width measurements to the designed width are plotted in **Figure S2** in Supplementary File. **Figure S2** (Supplementary File) clearly shows the

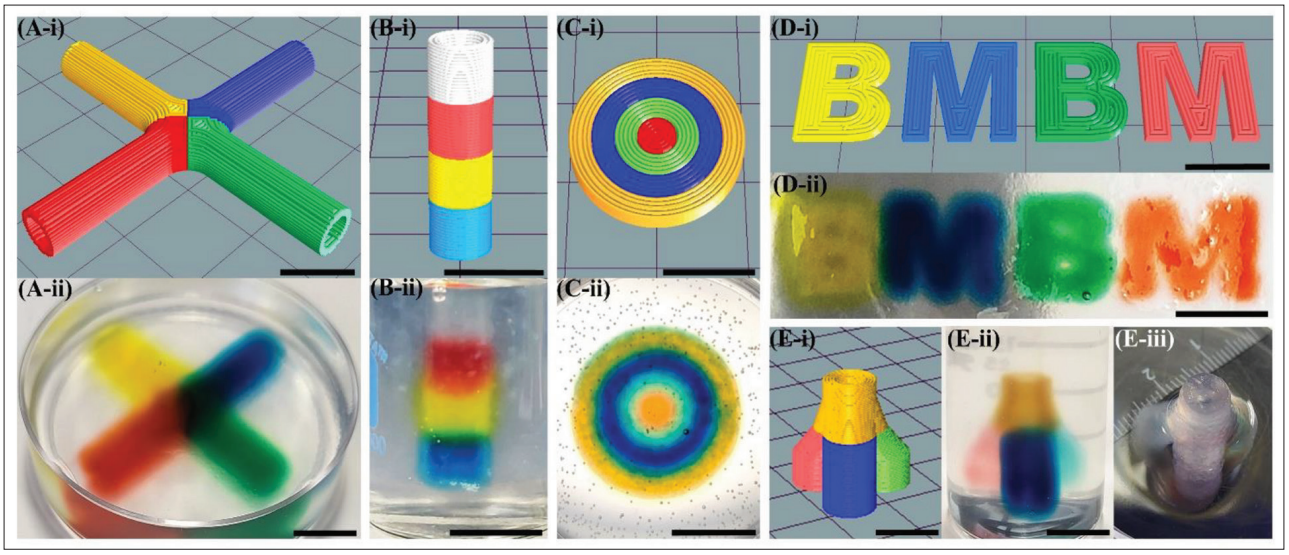

Figure 3. Support bath printing (SBP) toolpaths and prints. (A-i) G-code of a 40 × 40 × 5 mm 4-way intersection network of hollow tubes representing a capillary network. (A-ii) Printed 40 × 5 mm 4-way intersection network of hollow tubes in the support bath. (B-i) G-code of four 5 × 5 × 5 mm stacked hollow cylinders. (B-ii) Four printed 5 × 5 × 5 mm stacked hollow cylinders in the support bath. (C-i) G-code of a 4 multi-material 18 × 18 × 3 mm concentric cylinders. (C-ii) Printed 4 multi-material 18 × 18 × 3 mm concentric cylinders in the support bath. (D-i) G-code of a 48 × 10 × 1 mm BMBM lab signage in 4 different materials. (D-ii) Printed 45 × 10 × 1 mm BMBM lab in 4 different materials in the support bath. (E-i) G-code of 17 × 17 × 18 mm hollow trifurcation representing a capillary 3-to-1 merger. (E-ii) Printed 17 × 17 × 18 mm hollow trifurcation representing a capillary 3-to-1 merger in the support bath. (E-iii) Extracted 17 × 17 × 18 mm hollow trifurcation representing a capillary 3-to-1 merger from the support bath after crosslinking (color lost due to photobleaching after UV crosslinking) (scale bar = 1 cm applies to all images).

decreasing trend of significant change or deviation from the designed width as the temperature decreased and as printing was transitioned from the IAP to the SBP mode of operation. No significant change was observed between uncrosslinked and crosslinked constructs.

3.3.2. Cell viability, proliferation, and cell function

Cell viability and proliferation are important aspects that characterize the phenotype of the 3D-bioprinted constructs. To study the proliferation and viability, multiple cell-laden grid samples were printed and incubated in cell media at 37°C for 3 days. Cells were CFDA-SE-stained to allow the tracking of the cells over time. Samples were then stained with LIVE/DEAD staining and imaged with approximately 24-h gaps over the course of 3 days. As sown in Figure 5C and D, the proliferation of the HTR-8 cells could be realized at 24, 48, and 80 h after printing. It is clear how the cells are invading from the center toward the periphery of the printed strand, where nutrients can be accessed by the cells from the cell media. This provides a measure of cell proliferation within the printed construct. Figure 5E shows the LIVE/DEAD image overlays over areas within the printed structures, taken at 24, 48, and 80 h after printing. Cell viability rate was shown to be relatively high throughout the 80 h of incubation, averaging at 93.41%. **Figure S3** (Supplementary File) provides the quantitative data of the LIVE/DEAD measurements, showing how the viability was maintained above 90% over the time course of the assay with no significant loss in viability over the first couple of days. Most of the cells proliferated and formed clusters at the periphery of the printed GelMA where the supply of media was readily available. Subsequently, cells began to proliferate at the bottom of the petri dish around the printed hydrogel material. Some of the cells were observed to proliferate in clusters within the GelMA, while other very few cells remained stagnant and did not proliferate. Nevertheless, in the absence of staining of proliferation marker such as Ki67, proliferation can be detected by the significant increase in fluorescence intensity as time passes. We observed that the number of cells and fluorescence intensity increased over the 3-day time course study, as shown in Figure 5C-1, C-2, and C-3.

For cell functional assessment, the invasive phenotype of HTR-8 cells was studied. Figure 6C shows the final homogeneous outcome of the bioprinted placenta model. Three layers of GelMA were stacked and crosslinked separately as needed. Figure 6D shows an overlay of microscope FTIC and TRITC fluorescence images, and Figure 6E shows the different regions printed with the four different bioinks marked with dashed boxes with different colors. The red areas represent the EGF-laden GelMA bioinks. This composes the EGF module and the experimental channel in between. The white region represents the control channel that is comprised

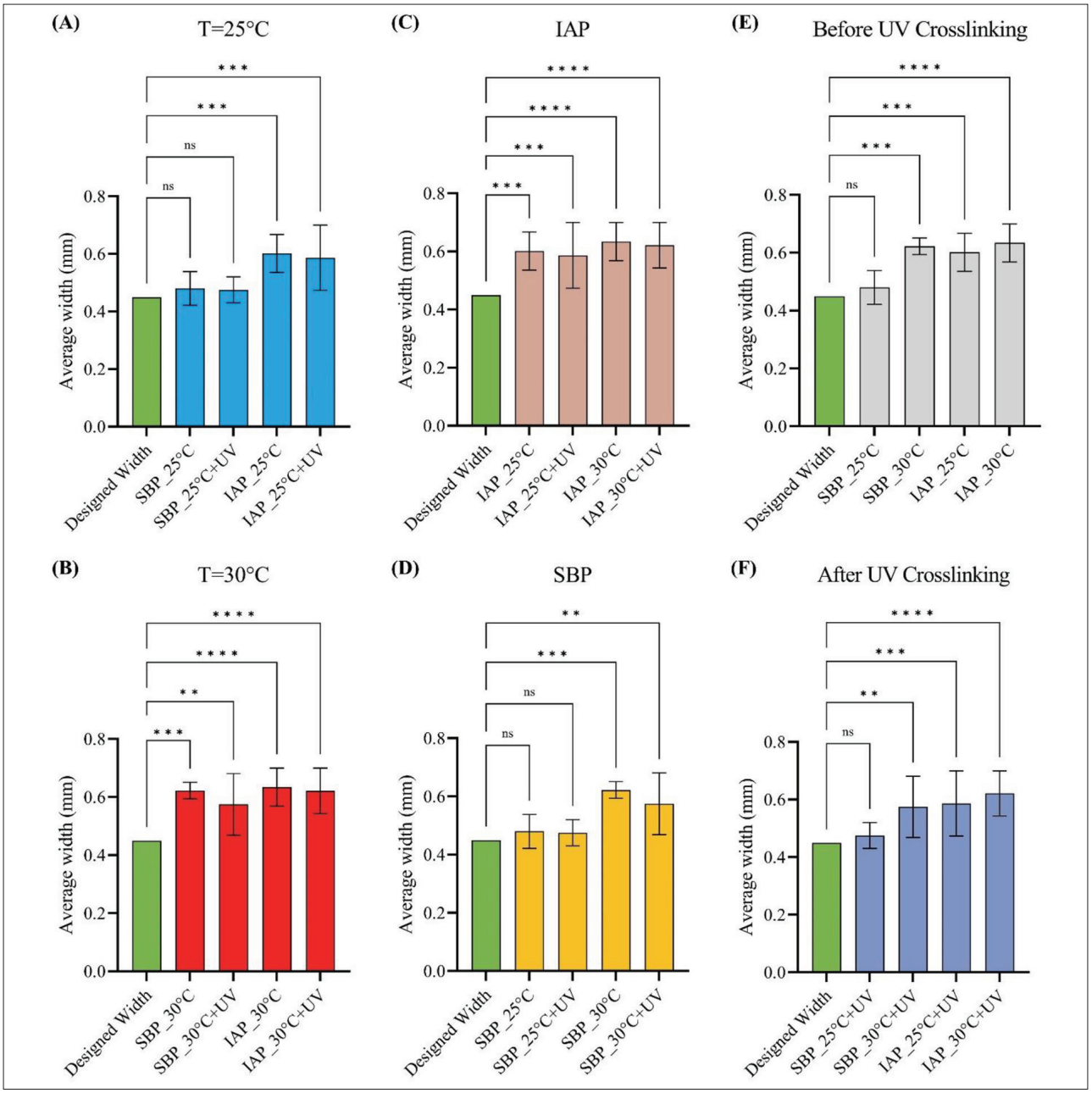

Figure 4. Average strand width measurements of grid scaffolds at different conditions. (A) Prints with bioink at room temperature T = 25°C. (B) Prints with bioink at T = 30°C. (C) Prints done with in-air printing (IAP). (D) Prints done with support bath printing (SBP). (E) Prints before UV crosslinking. (F) Prints after UV crosslinking. The green bar of each plot represents the designed strand width (0.45 mm).

of a GelMA bioink with no additives. The green region represents the HTR-8 cell module that sits parallel to the EGF module. Those two modules are separated by the two main control and experimental channels, as well as with highly crosslinked GelMA channels (yellow regions) that ensure the separation of modules and channels. In Figure 6F, a close-up image of the experimental channel shows the extent of HTR-8 invasion into this channel that contains EGF after 30 h. The average invasion distance into the channel was measured to be around 481.11 ± 74.55 μm, as compared to no invasion seen in the control channel that contains no EGF.

4. Discussion

4.1. Process design considerations

One main advantage that the QEB offers is the maximization of the printing volume along with the maximization of the

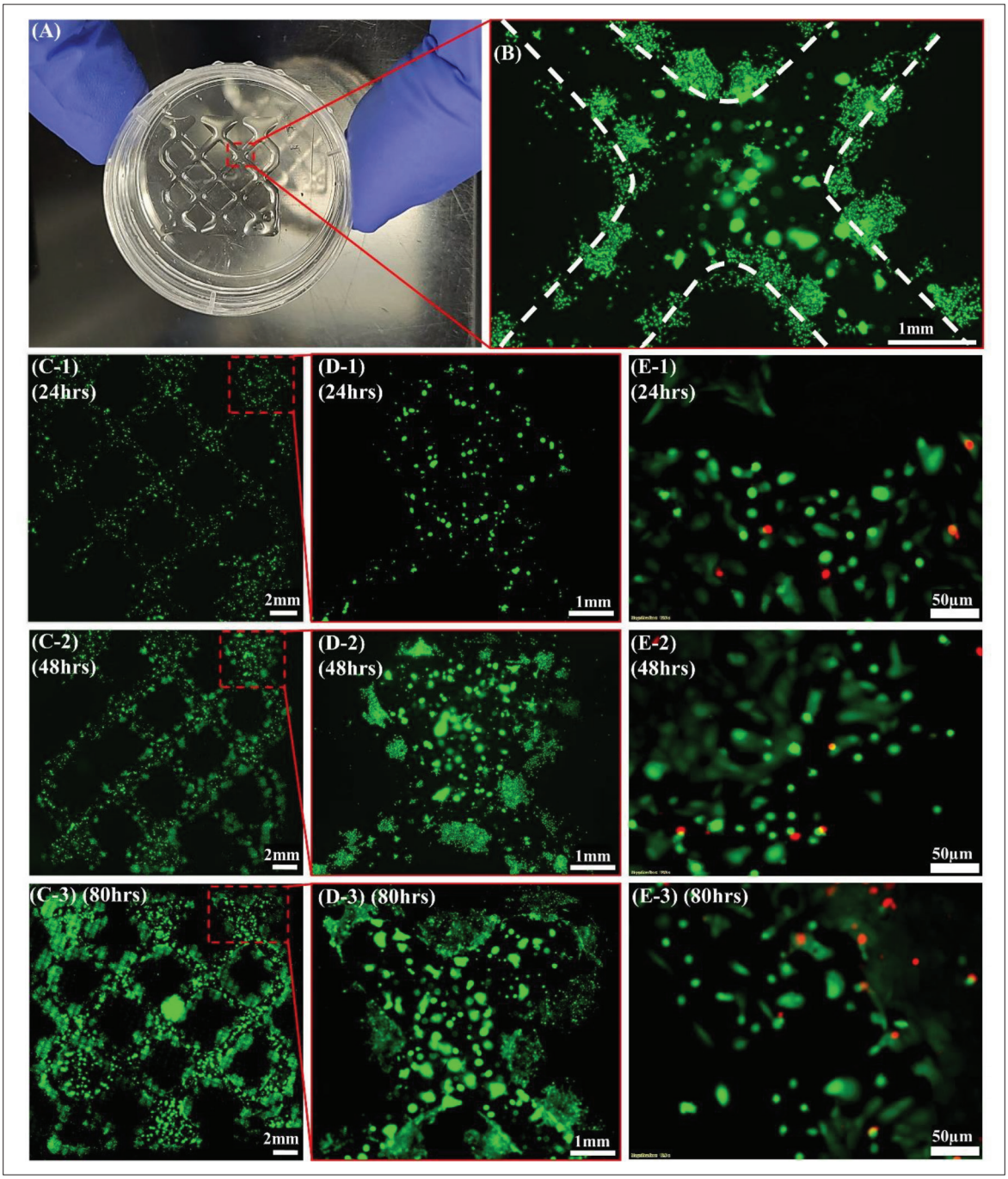

Figure 5. Cell viability and proliferation study. (A) 3D-printed 20 × 20 mm sample grid with 5% cell-laden GelMA. (B) Close-up of a strand crossing region at 48 h with white-dotted curves identifying the boundaries of the printed GelMA. (C-1) FITC fluorescence imaging of printed sample after LIVE staining at 24 h. (C-2) FITC fluorescence imaging of printed sample after LIVE staining at 42 h. (C-3) FITC fluorescence imaging of printed sample after LIVE staining at 80 h. (D-1) Close-up region of printed sample after 24 h. (D-2) Close-up region of printed sample after 42 h. (D-3) Close-up region of printed sample after 80 h. (E-1) LIVE/DEAD image overlay of a small region of the printed sample at 24 h after printing. (E-2) LIVE/DEAD image overlay of a small region of the printed sample at 42 h after printing. (E-3) LIVE/DEAD image overlay of a small region of the printed sample at 80 h after printing.

functionality and capabilities of the bioprinter. For example, when printing with four extruders in a single construct, the printing volume only reduces to 41.8% of the original printing volume of the Ender 3 Pro 3D printer as can be seen in Table 1. These sets of printable volumes achievable are relatively large with regard to the functionalities and capabilities offered in such a compact and low-cost bioprinter compared to other printers available in the

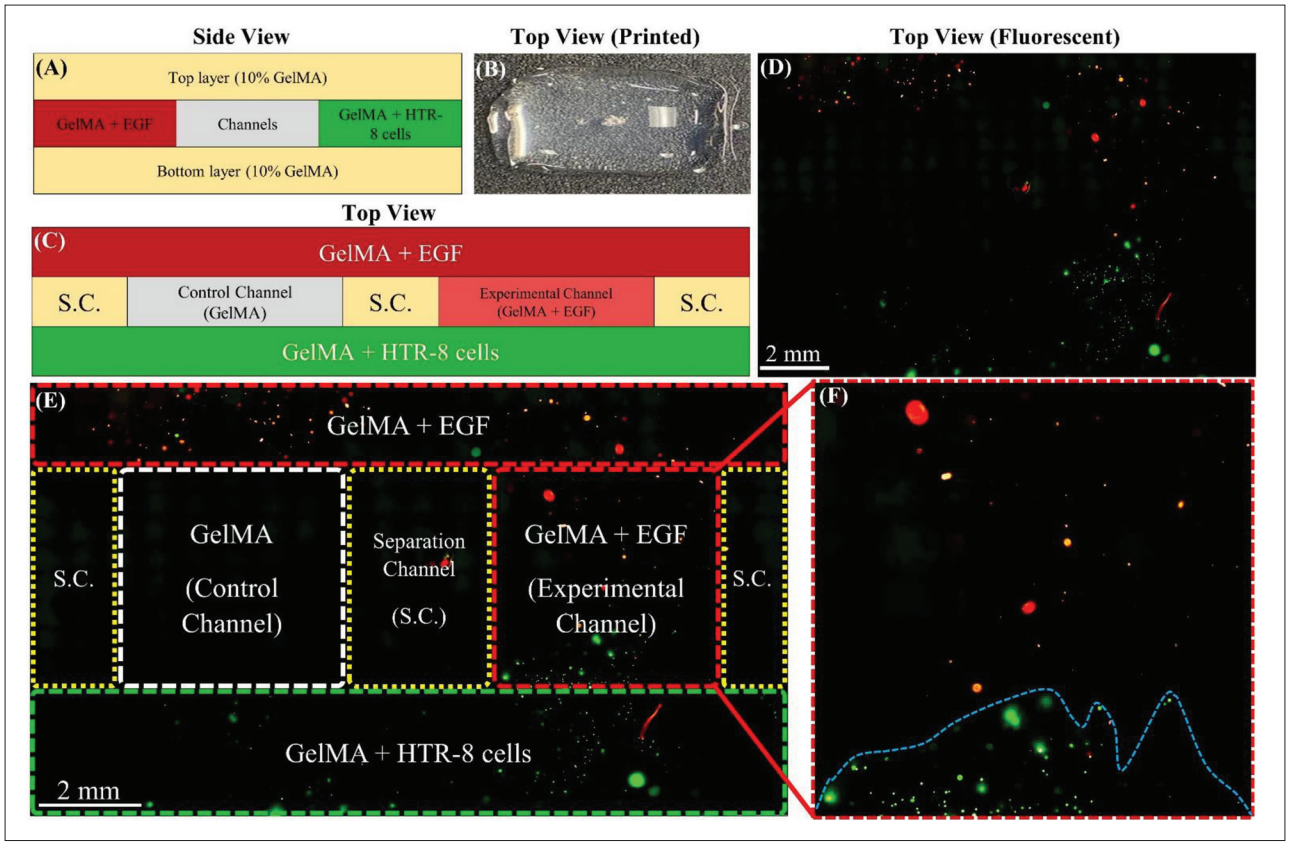

Figure 6. A 2-channel placenta model for HTR-8 cell invasion studies with 4 different bioinks. (A) Side view of the 2-channel placenta model with 4 different bioinks. (B) Top view of the 3D-bioprinted 2-channel placenta model. (C) Top view of the 2-channel placenta model showing the requirement of 4 different materials represented by 4 different colors (SC: separation channel). (D) FITC and TRITC fluorescence microscope images overlay showing the top view of the HTR-8 cells in green and epidermal growth factor (EGF) in red. (E) FITC and TRITC overlay with the different bioink areas within the bioprinted placenta model shown in different colors: Red dashed areas are the modules made of GelMA with EGF incorporated within; green dashed area is the module made of HTR-8 cells laden GelMA; white dashed area is the control channel composed of only GelMA; yellow dashed areas are the separation channels made of only highly crosslinked GelMA. (F) Close-up top view of the experimental channel composed of EGF-laden GelMA showing the invasion frontline of the HTR-8 cells within this channel represented by the dashed blue line.

literature and on the market[20-26]. For example, Kahl *et al.* were able to achieve a printing volume of approximately 20.66% with a single nozzle based on the original stock 3D printer configurations[27]. This is relatively small compared to the 95.5% printing volume achievable with the QEH design presented herein.

This was achieved with careful design of the base where the whole QES attached to the *X*-axis carriage is designed to give the whole QES space to traverse the *X*-axis bar beyond the physical limits existing at its extremities. It is also noteworthy that the volume of the syringes that can be mounted onto the QEH is 3 mL compared to the 1 mL syringes implemented in other systems, providing more volume capability to print larger structures at scale. Moreover, it is important to appreciate the advantages conferred by the QEB at such a low price point. The large printing volumes and multi-material printing capabilities provide this open-source design a great advantage over other present designs at such a low-cost range. Such advantages enable microfluidic mixing and gradient printing that can be achieved with minor upgrades, thereby creating opportunities for a much wider range of applications that can be targeted using such a system.

Regarding printing resolution and accuracy, although the 3D printer presents high mechanical stepper motor resolution, this does not necessarily help to enable the bioprinting of biological tissue constructs with high accuracy. This is because the printing accuracy and shape fidelity of soft materials and hydrogel-based bioinks not only depend on the printer's stepper motor resolutions but also closely depend on the printed material's rheological and chemical properties[42]. With the presented mechanical resolution of the system, the bioprinted material properties are the dominant factors affecting the structural fidelity of the bioprinted outcomes. These outcomes can be assessed and evaluated either experimentally or computationally

developed by Bonatti *et al.* and Paxton *et al.*[43,44]. In the case of the QEB, the recommended range of viscosity of the bioink would be similar to the typical range of viscosities that are enabled by extrusion-based bioprinters ensuring printability and accuracy of bioprinted constructs. Typically, the viscosity ranges between 30 mPa·s and 6×10^7 mPa·s[45]. As a caveat, the range of 3D-bioprintable materials with the QEB is currently limited to hydrogels that are extrudable at temperatures between 20°C and 40°C. This is due to the lack of an active temperature control unit. However, a wide range of hydrogel materials can be utilized including, but not limited to, gelatin-based hydrogels, collagen-based hydrogel, Pluronic, polyethylene glycol (PEG), as well as other materials such as ultrastretchable double-network hydrogel materials[46,47].

Without the frame for the QEH, it is difficult to maintain a perfect alignment for the four nozzles along the *x*–*y* directions. This is due to the non-uniformity within the plastic syringes and the needle tips locked onto them manually. The misalignment would be greater and would cause more inaccuracies with longer needle tips that can misalign more with a small initial deviation starting from the needle fixture. To compensate for that and ensure negligible misalignments, a needle frame was designed and added to the QEH that forces all four syringes to have an aligned tip position, as can be seen in Figure 1D. With the needle frame mounted, minimal nozzle alignment is required in the *x*–*y* directions and the different materials printed align well side by side with minimal mixing at the boundaries. The different structures shown in Figures 2 and 3 with the different cases of IAP and SBP show that the QEH renders multi-material structures with well-defined boundaries and interfaces between the different bioinks. The nozzles Z-calibration process was done semi-automatically by moving the nozzles to a single point on the bed, where all the nozzles were calibrated to touch and have the same zero level at that point. This was done by the help of the variable screw Z-limit switch designed. It is noteworthy that even with the same needle tips, the Z-level of each needle tip would be different since the tips are manually attached to the Luer locks of the syringes. Thus, a perfect Z-level alignment cannot be attained all the time due to human errors, causing the Z-home level to vary every time with the change of syringes and needles. Thus, a Z-leveling solution needs to be devised. For that reason, a variable limit switch was designed and added to the QEB to help calibrate the Z-home level with every new set of syringes mounted, as can be seen in Figure 1E. The added extension part above the limit switch can be extended or retracted using a screw mechanism to allow the accommodation of different needle sizes.

It is noteworthy that the effect of induced shear stress on the cells is independent of the extruder design. The mechanism by which the QES extrudes material can be categorized as a piston-driven mechanical extrusion[48]. This extrusion mechanism was chosen given the lower associated cost compared to pneumatically controlled ones due to the higher costs associated with pneumatic controllers. The induced stresses are well studied in the literature computationally and analytically, and have shown that these induced stresses that cells experience depend mainly on the nozzle type, the interchangeable 3 mL syringe needle tips in the case of the QES developed herein, and the bioink material and its viscosity[23,48-52]. Hence, the developed QES has no risk of having additional damaging effects on the extruded cells.

4.2. IAP and SBP outcomes

IAP is a printing paradigm that enables the printing of basic structures including grids and scaffolds. Minimal post-processing is required, and high cell viability outcomes can be achieved. IAP post-processing is considered minimal compared to SBP post-processing, which requires at least two additional steps before retrieving the final printed construct, namely release and washing from the support bath. However, scaling up the layer numbers invariably presents a challenge when working with hydrogels specified at low material concentrations, i.e., ≤5% in the case of GelMA, since low structural fidelity has been observed at these concentrations[53-55]. Notably, printed bioinks will spread across the substrate and relinquish the designed structure. Also, with multi-material printing, the mixing of different bioinks at the interfaces will occur. This will result in undefined multi-material structural outcomes. Continuous crosslinking of the bioink during printing is a way to minimize the spreading and loss of the prescribed structural outcome. However, this would result in inconsistencies of mechanical properties within the construct due to the earlier extruded layers being subjected to multi-fold crosslinking times compared to the latter layers extruded. Alternatively, increasing the bioink concentration would help in maintaining a better structural outcome and allow increased layer numbers when printing. However, other issues may arise like the printability of the bioink and cell viability. At low temperatures, high-concentration bioinks make material extrusion prohibitive owing to the decreased gelation temperature and increased viscosity. Moreover, the range of cell types that can be incorporated within higher-concentration bioinks would be reduced. This is because not all cells can survive and function natively in microenvironments that are mechanically stiff and that have small micro-porous structures. This may cause a drastic decrease in viability with certain types of cells.

In the case of SBP, many of the aforementioned difficulties with scaling up IAP outcomes can be overcome. By leveraging the thixotropic properties of the support baths, the bioinks are well supported in their extruded locations and no mixing between different bioinks will occur. More well-defined boundaries and edges can be attained, even with bioinks of very low concentrations. The one-time crosslinking of the printed outcomes in SBP helps also to produce consistent mechanical properties across the whole construct. Although the food dye can be seen diffusing into the support bath, the printed material remains in its printed location. After crosslinking, the dye is photo-bleached and the crosslinked GelMA is what is finally left without being affected by the diffusion, as can be seen in Figure 3E-ii. Further images and a video of the bioprinted structures using SBP can be accessed via the GitHub link, under the folder "Support Bath Printing Outcomes," mentioned in the Availability of data section.

Some difficulties, however, may also arise with SBP. One issue would be the difficulty of extracting thin structures from the supporting bath without causing any damage to it. Post-processing damage is more likely to happen with constructs printed with low-concentration bioinks and thin structures. Moreover, within small hollow structures, the removal of the SBM would be a challenge without causing any damage to the construct. Interlayer adhesion between the different bioinks may be problematic in the case of multi-material printing if the bioinks have very different properties and compositions that do not allow them to adhere to each other at the boundaries. This makes SBP a less favorable candidate for biological assays for thin multi-material structures, such as grids or scaffolds. The additional post-processing requirements may add more strains on cell viability due to the extended times when cells reside outside the physiological incubator conditions. It is noteworthy that the images presented in Figures 2 and 3 are qualitative and serve as evidence of functionality of the QEB developed. However, more quantitative studies are being conducted in conjunction with material parameters, which are needed to understand and optimize the bioprinting outcome of multi-material constructs.

4.3. Structural characterization

In order to characterize the structural fidelity of the printed outcomes using the QEB, measurements of printed grid structures, composed of 5% GelMA bioink, were carried out under different conditions as previously mentioned. It is apparent that at 25°C, the bioink exhibits a slightly higher viscosity that allows it to maintain a structure close to that of the designed one compared to the samples printed at 30°C. This can also be visualized by the average percent increase in strut width from the designed width of 0.45 mm (based on the nozzle diameter) for each of the different cases printed at 25°C vs. 30°C. The significant differences between the IAP and SBP measurements are caused by the bioink extruded into the support bath being withheld by the effect of the thixotropic properties of the SBM that helps maintain the extruded shape. In comparison, in IAP, the absence of any support medium around the extruded bioink on a substrate in the air leaves the bioink free to spread around the substrate, leading to a deterioration in its designed shape. This is more clearly realized when printing at GelMA bioink concentrations of 5% or less. Regarding the effect of UV crosslinking, the difference between the measurements before and after UV crosslinking still exists, although it is not very significant. This may be due to the bonds formed, as well as the slight dehydration that may happen within the GelMA, causing the volume/width to shrink compared to that before UV crosslinking. It can be deduced that the structures printed using SBP techniques, at 25°C, and that are UV-crosslinked show the closest compliance to the designed CAD model. Geometric design fidelity is a multi-faceted issue that is affected by multiple parameters at once. In addition to the tested parameters above, it is observed that the structural fidelity is highly affected by material and process parameters, including the temperature and concentration of the bioink, along with the SBM and the printing speed. Thus, further parametric studies that identify the optimal values for the different printing techniques would be valuable in creating a guide for multi-material printing with reliable outcomes. The bioink properties are among the parameters that affect the shape fidelity of the bioprinted construct. Relevant work includes a study by Ouyang *et al.* regarding the effect of bioink properties on printability and cell viability for 3D bioplotting of embryonic stem cells[56].

4.4. Biological characterization

The HTR-8 cells used to formulate the cell-laden bioinks are invasive cells and are capable of breaking down the hydrogel they are embedded in and invading in certain directions where a better supply of nutrients and chemoattracting factors would exist. Figures 5B and D clearly show the proper expected invasive behavior of the HTR-8 trophoblasts embedded in the GelMA constructs throughout the 3 days of incubation. The cells invaded the periphery of the GelMA boundaries, where they started to proliferate more extensively and easily with the abundant availability of cell media. This is also proven by the fact that the core of the printed strands carried a minimal number of cells, mainly dead cells, after 80 h of incubation. The samples imaged over time show a clear development of the number of cells, which is realized by the increased green fluorescence in the bioprinted constructs over time. Also, the shape extensions of cells

and their attachments with each other prove that the great majority of the cells are viable and are carrying on with their proper intended functions. One main function is the ability to invade through microenvironments by secreting matrix metalloproteinases (MMPs) that break down the microenvironment and open paths toward more favorable environments[35]. The relatively high cell viability average over 3 days (93.41%) illustrates the QEB process reliability in maintaining cell viability and function while preserving sterility. Given that cell viability and bioactivity highly depend on the material properties rather than the fabrication apparatus, this short-term viability assay helps determine the biocompatibility and efficacy of the developed QEB. If the QEB yields increased damage to the cells upon printing, this can be observed after printing over the course of this assay. It is evident that the initial cell viability is unaffected by the QEB printing process and is comparable to other studies that utilize GelMA[54]. Currently, more biological characterization is being done on constructs bioprinted with the QEB.

With the QEB process, the design, build, and establishment of a new *in vitro* placental model of trophoblast cell invasion are reported herein and illustrated in Figure 6. The presented placenta model comprises mainly four different material compositions and would be possible to print with the QEB developed. As shown in Figure 6A and B, the bottom and top cap, as well as the separation channels, are made of 10% GelMA to ensure that the HTR-8 cells would not invade or migrate through them. Alternatively, the cell and EGF modules, as well as the channels, are composed of 3% GelMA containing different constituents. The cell module includes HTR-8 cells within the 3% GelMA, and the EGF module contains a 16 μM concentration of EGF within the 3% GelMA. The experimental channel includes a lower EGF concentration of 4 μM, while the control channel is solely made up of 3% GelMA. Based on an earlier prototype model that incorporates the invasive phenotype of the HTR-8 cell line, the effect of gradient EGF concentrations on trophoblast invasion behavior has been previously established. Specifically, EGF has been shown to act as a chemoattractant for HTR-8 cells, driving the invasion toward regions of increasing concentrations of EGF[35]. Herein, a new multi-material, multi-compartmental model is advanced, thereby serving as an exemplar for the QEB fabrication of functional multi-material constructs that facilitate the study of cellular phenotypes under variable conditions. The invasion rate of the HTR-8 cells was observed to be significantly higher in the experimental channel compared to the control channel. With time, it is expected that the high concentration of EGF within the EFG module would start to diffuse into the two main channels. Thus, this diffusion would create a gradient of EGF within the bioprinted construct that drives the invasion of the HTR-8 cells into the opposing EGF module.

Since the HTR-8 cells are a heterogeneous cell line consisting of trophoblasts and stromal cells[57,58], staining for specific markers would be necessary to distinguish between the two cell populations found in the HTR-8 cell line that express the invasive phenotype. This would also help determine which cell type was proliferating more and which one formed cell clusters at the periphery of the bioprinted grids shown in Figure 5. The invasion is part of an ongoing placental study that addresses certain pregnancy dysfunctions, including pre-eclampsia and placenta accreta[35,59]. Overall, the data presented in Figure 6 highlight a biological test case that is an application of a multi-material construct enabled by the developed QEB. This work is currently being expanded and further studied to fully support and establish the EGF gradient within a 3D multi-material, multi-compartment 3D-bioprinted model that promotes the HTR-8 cell-invasive phenotype.

5. Limitations and future outlooks

From a hardware standpoint, one limitation of the in-line QEH design is the difficulty of alignment and calibration of the nozzles. Alignment and calibration are required in advance of each print and after the change of syringes. In the absence of proper alignment and calibration, slight misalignments within the printed construct would arise and would compromise the structural fidelity. The additional time required for calibration and alignment would also negatively affect the cellular viability outcome, as cells are removed from their optimal environment for longer times. This problem is currently being resolved by the development of a microfluidic head attachment that can be added to the QEH, allowing the precise printing of separate bioinks or a mixture of different bioinks through a single nozzle. This helps overcome the disadvantages in the current design and also in the other current designs in the literature. Aspects such as printing volume, misalignments between different nozzle tips, and multi-material mixing and gradient structures printing are tackled and will become a major advantage with this further upgrade of the QEB. Microfluidic printing and gradient mixing is a impactful field that is currently being optimized computationally[13], and practical implementation of such computational optimizations would be enabled by the low-cost microfluidic upgrade of the QEB. Another advantage of developing different microfluidic print heads is the facile adaptation of coaxial and multi-axial bioprinting. This is particularly useful for different materials that require additional additives for crosslinking, like $CaCl_2$ to chemically crosslink alginate-

based hydrogels, as well as different applications such as vascular constructs. Moreover, the QEH is being modified to be able to accommodate syringes with larger volumes for more scaled-up tissue models and organs. Furthermore, to enable further capabilities of reliable non-planar 3D bioprinting, a three-axis rotary stage is being designed and developed. This would render a substrate that can rotate to keep the nozzle orthogonal to the non-planar printing surface of pre-existing or pre-printed structures.

For more accurate structural outcomes, it is important to be able to precisely control the material parameters involved in bioprinting. From a material standpoint, one main material property to be tuned would be the bioink viscosity, which is controlled by the bioink temperature. The optimum viscosity value can then be transferred to other types of bioink material by controlling the bioink temperature. To realize and attain the desired bioink viscosity, an *in situ* viscosity measurement system is currently being developed to allow the determination of that optimal viscosity value, from which the temperature to be set would be known and actively controlled during printing. This is being done in conjunction with real-time image processing and machine learning algorithms to verify the compliance of the printed structures with the designed CAD models. This would enable a better flow of bioink with enhanced structural fidelity. To be sure, due to the lack of temperature control and different printing mechanisms, the QEB would be limited with the range of different materials it can process, including thermoplastics and other hard materials that can be used for biological applications.

Another limitation of multi-material printing is the interlayer adhesion strength between different material interfaces. This may be caused by the different properties and constituents of the different materials. To overcome such limitations, different design approaches can be followed, like the modification of CAD models and toolpaths, to account for the weak interfacial adhesion. This can be done by setting a small inset at the multi-material interfaces to allow stronger bonding and links between the different bioinks at boundary interfaces.

With the aforementioned developments, along with the expansion of the QEH to make it modular and compatible with several extrusion mechanisms, the scalability of the QEB would become possible with the added attributes such as increased reliability, robustness, and versatility. This would facilitate significant contributions to various engineered tissue applications that are currently out of the reach of current bioprinting capabilities. Moreover, in order to translate bioprinting studies into clinical use, it will be necessary to ensure process reliability with validation testing toward satisfying the requirements and regulations that render the bioprinter to be compliant with the current Good Manufacturing Practices (cGMP) as set by federal agencies, such as the U.S. Food and Drug Administration (FDA).

6. Conclusion

In this work, a low-cost quad-extrusion multi-material bioprinter was initially derived from an off-the-shelf desktop 3D printer, Creality Ender 3 Pro. The developed QEB was designed and fabricated in-house and validated through several printed structures using two different printing paradigms, namely, IAP and SBP. The novel design enables multi-material bioprinting at a very low cost, overcoming the issues of affordability and scalability that currently hamper the present designs as reported in current literature. Moreover, the challenges that traditionally accompany multi-material printing, like nozzle alignment, calibration, and diminished printing volumes, are overcome with the compactness of the bioprinter design presented herein. In addition to the latter advantages, the QES developed can be transferred to any other open-frame desktop 3D printer to render a fully functional bioprinter. Moreover, the bioprinted constructs produced under variable process conditions are then characterized structurally and biologically to verify the geometric fidelity of the bioprinted outcomes, as well as cell viability and cell function within those constructs. This signifies a great step further toward the availability and affordability of additive manufacturing for biological applications since the current techniques and technologies are still complex and at a very high cost. With the advancement of this QEB, it becomes feasible to extend the reach of such life-changing technologies to the general public at an accessible price point.

Further development to the QEB is under progress to include an onboard UV light source attached adjacent to the nozzle that allows instant crosslinking, either during or after printing. Also, an active heating system that allows precise control of the bioink and support bath (SB) temperatures, in combination with a real-time viscosity measurement system, is being developed to optimize the bioink viscosity that would render the best structural outcomes. Furthermore, a microfluidic nozzle extension to the present QEH is being designed to allow the micro-mixing of the different materials that are amenable to render new bioinks with different combinations or gradients from the separate four bioinks. The QEB with these low-cost upgrades would even further expand the range of applications that can be achieved with such an affordable and capable extrusion system, with high reliability and repeatability.

Acknowledgments

None.

Funding

The research was funded by the U.S. Army Medical Research Acquisition Activity under Award No. USAMRAA-W81XWH-19-1-0158. Any opinions, findings, and conclusions, or recommendations expressed in this publication are those of the authors and do not necessarily reflect the views of the U.S. Army Medical Research Acquisition Activity.

Conflict of interest

The authors declare they have no competing interests.

Author contributions

Conceptualization: Ralf Zgeib, Xiaofeng Wang
Formal analysis: Ralf Zgeib
Funding acquisition: Robert C. Chang
Investigation: Ralf Zgeib, Xiaofeng Wang
Methodology: Ralf Zgeib
Resources: Robert C. Chang
Supervision: Robert C. Chang
Writing – original draft: Ralf Zgeib
Writing – review & editing: Ralf Zgeib, Ahmadreza Zaeri, Fucheng Zhang, Kai Cao, Robert C. Chang

Ethics approval and consent to participate

Not applicable.

Consent for publication

Not applicable.

Availability of data

The datasets generated and analyzed for this study are available upon request from the corresponding author.

In the GitHub repository (https://github.com/RalfZgeib/QEB_BioEX), the STL files, modified Marlin firmware, and detailed table of components of the QES can be found. Also, additional images of the bioprinted structures using SBP can be found under the folder "Support Bath Printing Outcomes."

Additional supporting material can be found in the Supplementary File accompanying this article. The supplementary material includes additional figures, tables, and extended results that provide further insights and enhance the understanding of the research presented in this paper.

References

1. Correia Carreira S, Begum R, Perriman AW, 2020, 3D bioprinting: The emergence of programmable biodesign. *Adv Healthc Mater*, 9(15): 1–14.

   https://doi.org/10.1002/adhm.201900554

2. Zhang Z, Wu C, Dai C, *et al.*, 2022, A multi-axis robot-based bioprinting system supporting natural cell function preservation and cardiac tissue fabrication. *Bioact Mater*, 18(February): 138–150.

   https://doi.org/10.1016/j.bioactmat.2022.02.009

3. Ramiah P, du Toit LC, Choonara YE, *et al.*, 2020, Hydrogel-based bioinks for 3D bioprinting in tissue regeneration. *Front Mater*, 7(April): 1–13.

   https://doi.org/10.3389/fmats.2020.00076

4. Mandrycky C, Wang Z, Kim K, *et al.*, 2016, 3D bioprinting for engineering complex tissues. *Biotechnol Adv*, 34(4): 422–434.

   https://doi.org/10.1016/j.biotechadv.2015.12.011

5. Zaeri A, Cao K, Zhang F, *et al.*, 2022, A review of the structural and physical properties that govern cell interactions with structured biomaterials enabled by additive manufacturing. *Bioprinting*, 26(January): e00201.

   https://doi.org/10.1016/j.bprint.2022.e00201

6. Moroni L, Boland T, Burdick JA, *et al.*, 2018, Biofabrication: A guide to technology and terminology. *Trends Biotechnol*, 36(4): 384–402.

   https://doi.org/10.1016/j.tibtech.2017.10.015

7. Duan J, Cao Y, Shen Z, *et al.*, 2022, 3D bioprinted GelMA/PEGDA hybrid scaffold for establishing in-vitro model of melanoma. *J Microbiol Biotechnol*, 32(3): 531–540.

   https://doi.org/10.4014/jmb.2111.11003

8. Rostam-Alilou AA, Jafari H, Zolfagharian A, *et al.*, 2022, Experimentally validated vibro-acoustic modeling of 3D bio-printed grafts for potential use in human tympanic membrane regeneration. *Bioprinting*, 25(January): e00186.

   https://doi.org/10.1016/j.bprint.2021.e00186

9. Naghieh S, Lindberg G, Tamaddon M, *et al.*, 2021, Biofabrication strategies for musculoskeletal disorders: Evolution towards clinical applications. *Bioengineering*, 8(9).

   https://doi.org/10.3390/bioengineering8090123

10. Yu HW, Kim BS, Lee JY, *et al.*, 2021, Tissue printing for engineering transplantable human parathyroid patch to improve parathyroid engraftment, integration, and hormone secretion in vivo. *Biofabrication*, 13(3).

    https://doi.org/10.1088/1758-5090/abf740

11. Hwang DG, Jo Y, Kim M, *et al.*, 2022, A 3D bioprinted hybrid encapsulation system for delivery of human pluripotent stem cell-derived pancreatic islet-like aggregates. *Biofabrication*, 14(1).

    https://doi.org/10.1088/1758-5090/ac23ac

12. Celikkin N, Presutti D, Maiullari F, *et al.*, 2021, Tackling current biomedical challenges with frontier biofabrication and organ-on-a-chip technologies. *Front Bioeng Biotechnol*, 9(September): 1–26.

    https://doi.org/10.3389/fbioe.2021.732130

13. Zaeri A, Zgeib R, Cao K, *et al.*, 2022, Numerical analysis on the effects of microfluidic-based bioprinting parameters on the microfiber geometrical outcomes. *Sci Rep*, 12(1): 1–16.

    https://doi.org/10.1038/s41598-022-07392-0

14. Murphy CA, Lim KS, Woodfield TBF, 2022, Next evolution in organ-scale biofabrication: Bioresin design for rapid high-resolution vat polymerization. *Adv Mater*, 34 (February).

    https://doi.org/10.1002/adma.202107759

15. Kang YJ, 2020, Microfluidic-based biosensor for blood viscosity and erythrocyte sedimentation rate using disposable fluid delivery system. *Micromachines*, 11(2): 1–25.

    https://doi.org/10.3390/mi11020215

16. Kang HW, Lee SJ, Ko IK, *et al.*, 2016, A 3D bioprinting system to produce human-scale tissue constructs with structural integrity. *Nat Biotechnol*, 34(3): 312–319.

    https://doi.org/10.1038/nbt.3413

17. Mironov V, Kasyanov V, Markwald RR, 2011, Organ printing: From bioprinter to organ biofabrication line. *Curr Opin Biotechnol*, 22(5): 667–673.

    https://doi.org/10.1016/j.copbio.2011.02.006

18. Kang DH, Louis F, Liu H, *et al.*, 2021, Engineered whole cut meat-like tissue by the assembly of cell fibers using tendon-gel integrated bioprinting. *Nat Commun*, 12(1).

    https://doi.org/10.1038/s41467-021-25236-9

19. Ramachandraiah K, 2021, Potential development of sustainable 3d-printed meat analogues: A review. *Sustain*, 13(2): 1–20.

    https://doi.org/10.3390/su13020938

20. Warburton L, Lou L, Rubinsky B, 2022, A modular three-dimensional bioprinter for printing porous scaffolds for tissue engineering. *J Heat Transfer*, 144(3): 1–7.

    https://doi.org/10.1115/1.4053198

21. Tavafoghi M, Darabi MA, Mahmoodi M, *et al.*, 2021, Multimaterial bioprinting and combination of processing techniques towards the fabrication of biomimetic tissues and organs. *Biofabrication*, 13(4).

    https://doi.org/10.1088/1758-5090/ac0b9a

22. Tong A, Pham QL, Abatemarco P, *et al.*, 2021, Review of low-cost 3D bioprinters: State of the market and observed future trends. *SLAS Technol*, 26(4): 333–366.

    https://doi.org/10.1177/24726303211020297

23. Choudhury D, Anand S, Naing MW, 2018, The arrival of commercial bioprinters - Towards 3D bioprinting revolution! *Int J Bioprinting*, 4(2): 1–20.

    https://doi.org/10.18063/IJB.v4i2.139

24. Ravanbakhsh H, Karamzadeh V, Bao G, *et al.*, 2021, Emerging technologies in multi-material bioprinting. *Adv Mater*, 33(49).

    https://doi.org/10.1002/adma.202104730.

25. Zhang YS, Haghiashtiani G, Hübscher T, *et al.*, 2021, 3D extrusion bioprinting. *Nat Rev Methods Prim*, 1(1): 75.

    https://doi.org/10.1038/s43586-021-00073-8

26. Shen EM, McCloskey KE, 2021, Affordable, high-resolution bioprinting with embedded concentration gradients. *Bioprinting*, 21(October 2020): e00113.

    https://doi.org/10.1016/j.bprint.2020.e00113

27. Kahl M, Gertig M, Hoyer P, *et al.*, 2019, Ultra-low-cost 3D bioprinting: Modification and application of an off-the-shelf desktop 3D-printer for biofabrication. *Front Bioeng Biotechnol*, 7(JUL): 1–12.

    https://doi.org/10.3389/fbioe.2019.00184

28. Wagner M, Karner A, Gattringer P, *et al.*, 2021, A super low-cost bioprinter based on DVD-drive components and a raspberry pi as controller. *Bioprinting*, 23(November 2020): e00142.

    https://doi.org/10.1016/j.bprint.2021.e00142

29. Pusch K, Hinton TJ, Feinberg AW, 2018, Large volume syringe pump extruder for desktop 3D printers. *HardwareX*, 3: 49–61.

    https://doi.org/10.1016/j.ohx.2018.02.001

30. Krige A, Haluška J, Rova U, 2021, Design and implementation of a low cost bio-printer modification, allowing for switching between plastic and gel extrusion. *HardwareX*, 9: e00186.

    https://doi.org/10.1016/j.ohx.2021.e00186

31. Yenilmez B, Temirel M, Knowlton S, *et al.*, 2019, Development and characterization of a low-cost 3D bioprinter. *Bioprinting*, 13(December 2018): e00044.

    https://doi.org/10.1016/j.bprint.2019.e00044

32. Bessler N, Ogiermann D, Buchholz MB, *et al.*, 2019, Nydus one syringe extruder (NOSE): A Prusa i3 3D printer conversion for bioprinting applications utilizing the FRESH-method. *HardwareX*, 6: e00069.

    https://doi.org/10.1016/j.ohx.2019.e00069

33. Tashman JW, Shiwarski DJ, Feinberg AW, 2021, A high performance open-source syringe extruder optimized for extrusion and retraction during FRESH 3D bioprinting. *HardwareX*, 9(2021): e00170.

https://doi.org/10.1016/j.ohx.2020.e00170

34. Garciamendez-Mijares CE, Agrawal P, García Martínez G, *et al.*, 2021, State-of-art affordable bioprinters: A guide for the DiY community. *Appl Phys Rev*, 8(3): 47818.

https://doi.org/10.1063/5.0047818

35. Ding H, Illsley NP, Chang RC, 2019, 3D bioprinted GelMA based models for the study of trophoblast cell invasion. *Sci Rep*, 9(1): 1–14.

https://doi.org/10.1038/s41598-019-55052-7

36. Salahuddin B, Wang S, Sangian D, *et al.*, 2021, Hybrid gelatin hydrogels in nanomedicine applications. *ACS Appl Bio Mater*, 4(4): 2886–2906.

https://doi.org/10.1021/acsabm.0c01630

37. Li H, Tan YJ, Kiran R, *et al.*, 2021, Submerged and non-submerged 3D bioprinting approaches for the fabrication of complex structures with the hydrogel pair GelMA and alginate/methylcellulose. *Addit Manuf*, 37(October 2020): 101640.

https://doi.org/10.1016/j.addma.2020.101640

38. S. Alsoufi M, W. Alhazmi M, K. Suker D, *et al.*, 2019, Experimental characterization of the influence of nozzle temperature in FDM 3D printed pure PLA and advanced PLA+. *Am J Mech Eng*, 7(2): 45–60.

https://doi.org/10.12691/ajme-7-2-1

39. Zhu W, Qu X, Zhu J, *et al.*, 2017, Direct 3D bioprinting of prevascularized tissue constructs with complex microarchitecture. *Biomaterials*, 124(April 2017): 106–115.

https://doi.org/10.1016/j.biomaterials.2017.01.042.Direct

40. Ding H, Chang RC, 2018, Printability study of bioprinted tubular structures using liquid hydrogel precursors in a support bath. *Appl Sci*, 8(3).

https://doi.org/10.3390/app8030403

41. Gu Y, Schwarz B, Forget A, *et al.*, 2020, Advanced bioink for 3D bioprinting of complex free-standing structures with high stiffness. *Bioengineering*, 7(4): 1–15.

https://doi.org/10.3390/bioengineering7040141

42. Schwab A, Levato R, D'Este M, *et al.*, 2020, Printability and shape fidelity of bioinks in 3D bioprinting. *Chem Rev*, 120(19): 11028–11055.

https://doi.org/10.1021/acs.chemrev.0c00084

43. Bonatti AF, Chiesa I, Vozzi G, *et al.*, 2021, Open-source CAD-CAM simulator of the extrusion-based bioprinting process. *Bioprinting*, 24(July): e00172.

https://doi.org/10.1016/j.bprint.2021.e00172

44. Paxton N, Smolan W, Böck T, *et al.*, 2017, Proposal to assess printability of bioinks for extrusion-based bioprinting and evaluation of rheological properties governing bioprintability. *Biofabrication*, 9(4).

https://doi.org/10.1088/1758-5090/aa8dd8

45. Hölzl K, Lin S, Tytgat L, *et al.*, 2016, Bioink properties before, during and after 3D bioprinting. *Biofabrication*, 8(3).

https://doi.org/10.1088/1758-5090/8/3/032002

46. Suntornnond R, An J, Chua CK, 2017, Bioprinting of thermoresponsive hydrogels for next generation tissue engineering: A review. *Macromol Mater Eng*, 302(1).

https://doi.org/10.1002/mame.201600266

47. Li H, Zheng H, Tan YJ, *et al.*, 2021, Development of an ultrastretchable double-network hydrogel for flexible strain sensors. *ACS Appl Mater Interfaces*, 13(11): 12814–12823.

https://doi.org/10.1021/acsami.0c19104

48. Boularaoui S, Al Hussein G, Khan KA, *et al.*, 2020, An overview of extrusion-based bioprinting with a focus on induced shear stress and its effect on cell viability. *Bioprinting*, 20(August): e00093.

https://doi.org/10.1016/j.bprint.2020.e00093

49. Liu W, Heinrich MA, Zhou Y, *et al.*, 2017, Extrusion bioprinting of shear-thinning gelatin methacryloyl bioinks. *Adv Healthc Mater*, 6(12): 1–11.

https://doi.org/10.1002/adhm.201601451

50. Emmermacher J, Spura D, Cziommer J, *et al.*, 2020, Engineering considerations on extrusion-based bioprinting: interactions of material behavior, mechanical forces and cells in the printing needle. *Biofabrication*, 12(2).

https://doi.org/10.1088/1758-5090/ab7553

51. Han S, Kim CM, Jin S, *et al.*, 2021, Study of the process-induced cell damage in forced extrusion bioprinting. *Biofabrication*, 13(3).

https://doi.org/10.1088/1758-5090/ac0415

52. Poologasundarampillai G, Haweet A, Jayash SN, *et al.*, 2021, Real-time imaging and analysis of cell-hydrogel interplay within an extrusion-bioprinting capillary. *Bioprinting*, 23(May): e00144.

https://doi.org/10.1016/j.bprint.2021.e00144

53. Boularaoui S, Shanti A, Lanotte M, *et al.*, 2021, Nanocomposite conductive bioinks based on low-concentration GelMA and MXene nanosheets/gold nanoparticles providing enhanced printability of functional skeletal muscle tissues. *ACS Biomater Sci Eng*, 7(12): 5810–5822.

https://doi.org/10.1021/acsbiomaterials.1c01193

54. Yin J, Yan M, Wang Y, *et al.*, 2018, 3D bioprinting of low-concentration cell-laden gelatin methacrylate (GelMA)

bioinks with a two-step cross-linking strategy. *ACS Appl Mater Interfaces*, 10(8): 6849–6857.

https://doi.org/10.1021/acsami.7b16059

55. Xu W, Molino BZ, Cheng F, *et al.*, 2019, On low-concentration inks formulated by nanocellulose assisted with gelatin methacrylate (GelMA) for 3D printing toward wound healing application. *ACS Appl Mater Interfaces*, 11(9): 8838–8848.

https://doi.org/10.1021/acsami.8b21268

56. Ouyang L, Yao R, Zhao Y, *et al.*, 2016, Effect of bioink properties on printability and cell viability for 3D bioplotting of embryonic stem cells. *Biofabrication*, 8(3): 035020.

https://doi.org/10.1088/1758-5090/8/3/035020

57. Abou-Kheir W, Barrak J, Hadadeh O, *et al.*, 2017, HTR-8/SVneo cell line contains a mixed population of cells. *Placenta*, 50: 1–7.

https://doi.org/10.1016/j.placenta.2016.12.007

58. Msheik H, Azar J, El Sabeh M, *et al.*, 2020, HTR-8/SVneo: A model for epithelial to mesenchymal transition in the human placenta. *Placenta*, 90(September 2019): 90–97.

https://doi.org/10.1016/j.placenta.2019.12.013

59. Kuo CY, Eranki A, Placone JK, *et al.*, 2016, Development of a 3D printed, bioengineered placenta model to evaluate the role of trophoblast migration in preeclampsia. *ACS Biomater Sci Eng*, 2(10): 1817–1826.

https://doi.org/10.1021/acsbiomaterials.6b00031